Analysis of water droplet penetration in earth plasters using X-ray microtomography

T. Mauffre, E. Keita, Elise Contraires, F. Mcgregor, A. Fabbri

Analysis of water droplet penetration in earth plasters using X-ray microtomography

T.Mauffré (a,*) , E.Keita (b) , E.Contraires (c), F.McGregor (a), A.Fabbri (a)

a LGCB-LTDS, UMR 5513 CNRS, ENTPE, 3 Rue Maurice Audin, 69120 Vaulx-en-Velin, France

b Laboratoire Navier, Université Gustave Eiffel, ENPC, CNRS, Marne la Vallée, France

c TPCDI-LTDS, UMR 5513 CNRS, Ecole Centrale de Lyon, 36 Avenue Guy de Collongue, 69134 Écully, France

∗ corresponding author. email address: mauffre.thibaud@gmail.com

Highlights

- Water damping droplet penetration followed by original X-ray microtomography
- Spread, depth and quantity of the droplet monitored inside the earthen plaster
- Surface topography has a direct link with the inertial water penetration
- After impact, water behavior is only influenced by bulk properties of the plaster
- A clayish plaster prevents water to penetrate too deeply but has a slow drying rate

Abstract

Earth plasters are a very interesting solution for the coating of earthen construction, in terms of embodied energy, technical efficiency, while keeping the hygroscopic properties of the wall, unlike very little permeable coatings, as the cement-based ones. An experimental campaign has been conducted on several earth plasters which differs by their sand granulometry, earth origin and earth to sand ratio, leading to controlled surface topography and bulk properties. A novel X-ray microtomography technique adapted to such material has been relevant to observe directly the penetration of a water damping droplet inside the plaster with the 2D radiograph method, and enhance the understanding of the role of the surface and the bulk structure on it. A 3D scanning method was useful to understand the microstructure of the different samples and analyse their differences in terms of porosity. Two custom-made MATLAB codes have been developed in order to follow the droplet parameters inside the material, such as the spread, the penetration depth and the relative quantity of water along the time. Results show the consistent role of the surface topography on the water inertial penetration, while the penetration rate due to diffusion is directly linked to the bulk properties, and can be assimilated to a classic diffusion solution. The determination of the drying rate in the earth plasters highlights that the plasters which prevent the water to penetrate too deeply are also the ones which dry the slower, leading to a questioning on the role researched in an efficient coating material.

Keywords

Earth plasters; X-ray microtomography; water penetration; water damping; surface topography; drying rate.

1 Introduction

In the current context of global warming, there is a growing interest on the use of raw earth construction materials, [1;2]. This can be explained by their low embodied energy and carbon. As a building material, raw earth has been used for centuries, especially because of its availability, its high thermal inertia, and its hygroscopic properties [3;4;5;6]. However, earthen walls are very sensitive to water which can cause problematic phenomena as erosion [7] or mechanical weakening [8;9]. Earth plasters have nowadays the role to protect the earthen walls from erosion as a sacrificial layer, and to offer a thermal and sound protection to the housing, compatible with the rest of the earthen wall for the transfer of vapor. Recent researches have already focused on the efficiency of the plasters in terms of physical mechanical performances [10;11;12;13], or in terms of moisture absorption and adsorption [14]. Only few recent studies have shown interest on the capacity of the unstabilized earth plasters to resist to water projections in order to improve their durability [15;16].

A large amount of researches have already focused on the behavior of liquid water and vapor into earthen walls [17]. Yet, the absorption which occurs at the building facade is not well understood. Capillary penetration of liquids into porous media has been a subject of studies since many years already, and models for finite volume droplets on model materials have been developed using simple analytical solutions as in [18;19]. Studies on water droplet damping on porous surfaces and the droplet behavior after impact have recently been published [20;21;22]. However, literature still gives very few information about surface absorption on raw earth. Furthermore, raw earth is a complex material which adds several

issues as multi-scale roughness, pore size distribution, and strong clay adsorption. X-ray microtomography is a common technique to analyse the 3D microstructure of every kind of material. It can also be used to observe the presence of liquids inside these materials, leading to studies on water drying [23] or spatial variation of water saturation [24]. Very recently this technique has been used to observe quick phenomenon such as water movements inside the bulks [25].

The novelty of our approach is to consider surface topography of earthen plasters as an influential parameter on the raindrop's wettability and absorption. In this context, this paper aims to give an idea of the effect of the surface topography and bulk properties on the absorption of a water droplet on different earth plasters. For that purpose, earth plaster samples with a great variety of composition (granulometry, earth, clay), have been realized in order to obtain different surface topography and volume properties. An experimental device has been designed to follow the absorption of the water droplet inside the material by the technique of X-ray microtomography.

Finally, understanding the mechanisms of the absorption of water droplets on raw earth materials will allow innovative design of material texturing or formulation to reduce the vulnerability to moisture ingress. Buildings with unstabilized earthen materials exposed to water projections or rain would particularly benefit from advances made on increased surface durability.

2 Materials and methods

2.1 Material and sample preparation

Earth plaster samples with different surface topography and different volume composition were prepared to study the effect of both surface and bulk properties on the penetration of a water droplet damping. Based on classic recommendation for the earth/sand mix for earth plasters [26], sample compositions were designed in order to be sufficiently representative of a real earth plaster, with variations of the sand granulometry, the origin and amount of earth used. Theses formulations have been chosen among 20 formulations in order to obtain the highest variety of surface and volume properties, except for B1 and B2 to study the repeatability. The following Table 1 summarizes the composition of each sample.

Sample	Sand added granulometry	Earth (%)	Sand added (%)	Process Water (%)	Clay (%)	Earth Region
A1	0 - 315 µm	17	83	18.2	4.42	Dagneux
A3	315 - 630 µm	17	83	15.5	4.42	Dagneux
A5	630 - 1 mm	17	83	14.3	4.42	Dagneux
A9	0 - 2 mm	17	83	14.3	4.42	Dagneux
B1	0 - 630 µm	30	70	15.9	7.8	Dagneux
B2	0 - 630 µm	30	70	15.9	7.8	Dagneux
B1C	0 - 630 µm	30	70	16.3	11.4	Confluence
B1S	0 - 630 µm	30	70	21.7	16.5	STA
B5	0 - 630 µm	50	50	15.9	13	Dagneux

Table 1: Earth plasters composition

Clay percentage is the final quantity of clay within the plaster. The process water percentage refers to the percentage in mass of the plaster at the end of the fabrication. This quantity has been determined in order to get the same workability for all the plasters. Three different

types of raw earths, named according to their origin location, Dagneux, Saint-Antoine (STA) and Confluence, were tested. They all came from existing rammed earth constructions located in Rhône-Alpes region in the South-East of France. The earth was sieved to a very fine fraction of 60 µm with the help of water, then heated to 95°C maximum to avoid burning the clays, during 48 hours. The residue was then grinded with a small mobile crusher to obtain a fine powder again. The particle size distribution of all three raw earths was determined in accordance with the NF EN ISO 17892-4 norm [27]. Dagneux earth is composed of 26% of clay (in mass), while STA earth is composed of 55%, and Confluence earth 38%. The sand, coming from the French quarry La Petite Craz, was sieved into several different size fractions. The sieved sand and the sieved earth were first mixed manually dry together before adding the water. Then the plaster was poured manually into a cylindrical mold of 7 cm in diameter and 2 cm in height which was previously greased on the side and a filter paper was added at the bottom. The surface of the sample was then flattened with a metal spatula. The plasters were cured under controlled temperature (20°C) for at least two weeks before demolding. From the same mortar were produced two earth plaster samples. Indeed bulk properties were measured on the cylindrical samples, whereas the replicas were sawed into 2 cm cubes in order to have the right size for the X-ray microtomography.

The volumetric properties of each sample are presented in the Table 2. The density was calculated from the mass and volume of the dry sample after shrinkage. The samples volume was calculated based on dimensions measured with caliper. The water absorption coefficient (called A-value) by capillarity was determined using the EN 1015-18 norm [29] protocol for mortars, but modified for earth plaster samples. The design of the samples used for the A-value test is the same than presented before. In addition, the edges of the samples were coated with paraffin wax and then taped with aluminum tape. Only the top and the bottom

surface were free. Weighting measurements have been realized every 5 minutes during the water absorption. Porosity is determined for all samples by two successive tests. First with the pycnometer, the volume of the skeleton of the sample is measured thanks to the volume of azote under pressure injected in the cell containing the sample: the azote penetrates inside the porosity. Then the sample is coated with paraffin and weighted into water: the hydrostatic weighting gives its total volume. Thereafter, the relation between the porosity denoted *n*, the volume of the sample V_s and the volume of the skeleton of the sample V_{sk} is equal to:

$$n = \frac{V_s - V_{sk}}{V_s} \quad (1)$$

Sample	A1	A3	A5	A9	B1	B1C	B1S	B2	B5
Density (kg.m^{-3})	1660	1600	1650	1770	1820	1780	1700	1790	1830
A-value (kg.m^{-2}.s$^{-0.5}$)	0.156	0.087	0.104	0.106	0.082	0.080	0.046	0.082	0.066
Porosity (%)	30	32	25	26	26	18	22	26	27

Table 2: Bulk properties of the earth plasters sample

It can be noticed that the A-value for B1S is twice lower than for B1 and B1C. It indicates that the earth from STA has a lower capacity for the absorption of water by capillarity. As expected, the highest porosity rate is for the samples A1 and A3, which presents the lowest amplitude of grain size, and therefore a bad particle size staking. For the other samples, the porosity rate is quite stable around 26%, except for sample B1S and B1C, which are composed of a different earth. This result shows the influence of the earth origin on the porosity of the earth plaster.

2.2 Surface topography

The representative parameter for surface topography used in this study is the arithmetic roughness R_a. It represents the arithmetic average height of the sample profile. For all the samples, it was measured with the same experimental device (multi-chromatic confocal sensor (STILL, Everest CHR)) and protocol than in a previous study on compacted earth blocks [29]. It can be noticed that the range of values is high compared to the ones for the compacted earth blocks from [29] (from 15 to 24 µm). It shows the influence of the sand granulometry and the fabrication method on this parameter. The roughness values R_a for all the samples are reported in Table 3.

Sample	**A1**	**A3**	**A5**	**A9**	**B1**	**B1C**	**B1S**	**B2**	**B5**
R_a (µm)	16.4	28.7	29.3	23.5	11.7	14.5	9.3	13.8	5.2

Table 3: Arithmetic roughness R_a for all samples

2.3 X-ray microtomography

The X-ray micro computed tomography (microtomography) is a nondestructive technique to characterize material microstructure in two or three dimensions with a spatial resolution at the micron scale. The X-ray laboratory scanner used for this experiment was Ultratom from RX-Solution at Laboratoire Navier in France. A micro-focus X-ray source (Hamamatsu L10801) illuminates the object with a tension of 130 KV and a current of 100 µA. A flat-panel imager (Paxscan Varian, 1920 X 1560 pixels) recorded 16-bit 2D radiographs with a pixel size of 20 µm at 10 frames per second. The more the X-rays encounter matter, the more the X-ray intensity decreases. Therefore, the microtomography system can build 2D radiographs of

a porous or heterogeneous material with gray levels, based on X-ray attenuation directly linked to the chemical composition and density. In order to obtain a 3D scan of the material, an angular system rotates the object and, based on the 1440 images acquired for the whole sample, a computer reconstructed a 3D image of the object.

In this paper, both 2D radiograph and 3D scanning methods are used. It takes several hours, depending on the resolution of the image wanted, to get a stack of images, therefore it needs the material to stand still for all the duration of the scan. With the 3D scanning method, it is possible to measure the porosity of the material and its repartition along the sample, especially concerning the zone just under the surface. Meanwhile the 2D projection method is suitable to observe quick changes in the material. Indeed, it is possible to get several images per second with this method, depending on the signal to noise ratio. This makes it possible to follow the liquid water penetration through the surface.

3 Results

3.1 Development of the experimental set-up and adjustment of the X-ray microtomography parameters

The experimental set-up is shown in Figure 1. Using a water delivering system above the sample, a capillary tube is connected to a syringe pump (Harvard Apparatus). The capillary tube has a 500 µm internal diameter, the water droplet falls from the tube when its mass is higher than the capillary forces, creating a 12 µl volume droplet. The distance between the capillary tube and the surface of the sample is 5.5 cm, in order to get a droplet speed at impact around 1 m/s. This speed is sufficient to get a correct spread and slow enough to avoid the droplet's bursting.

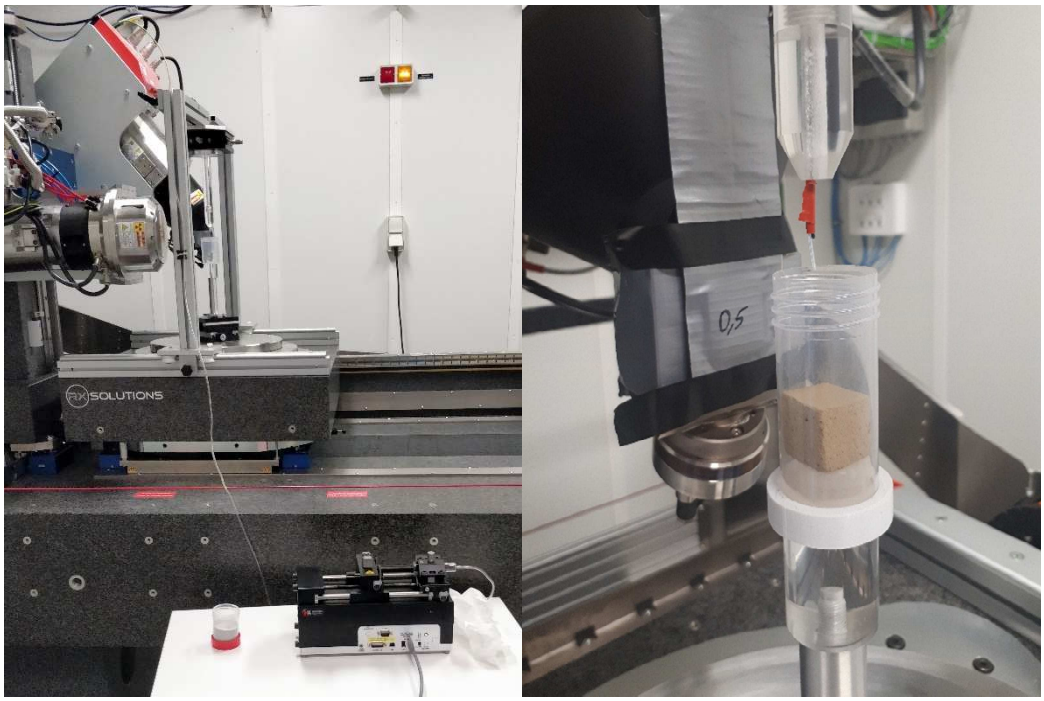

Figure 1: Experimental water damping set-up (left), zoom on the sample, source and capillary (right)

The size of the sample, a 2 cm cube, is relatively small, but it is sufficiently representative of the micro and macro structure of the earth plaster, since it is more than ten times larger than the size of the largest particle of the plaster (gravel around 630 µm). With this small size, the X-ray source can be positioned close to the core of the sample, allowing a better resolution of the detected image. The shape of the sample is chosen cubic in order to avoid beam hardening. Indeed, with a cylindrical sample, radiographs may exhibit beam hardening artefacts as the X-ray beam go through less matter on the edge. To further reduce this artefact, copper sheet of 0.5mm has been added in front of the X-ray source, thus low energy X-rays are stopped. These precautions are mandatory, because we did not use image for morphological study but we used the gray value from radiographs to quantify the density of the sample and the distribution of water.

200 The pixel size was set at 20 µm and the image acquisition at 10 frames per second (fps). To
201 capture the water imbibition, we needed a field of view of 3 cm. To better detect the
202 surface, it is positioned in the center of the screen, thus we used only half the image.
203 Therefore, the pixel size is a relatively high value. The frame rate is limited by the Hard Drive
204 writing speed; indeed, each image is over 4.26 Mo. Moreover, a higher frame rate would
205 have decreased the signal to noise ratio and thus the image quality, making it more difficult
206 to identify the water within the material. Only one droplet is released at the surface of the
207 sample, and the recording time is 23 minutes. The recorded data is very important due to
208 the high-resolution images. Consequently, a short computer program has been created to
209 change the frame rate acquisition from 10 fps to 1 fps after 3 minutes, in order to avoid the
210 saturation of the storage capacity. To reduce the frame rate, the acquisition parameters are
211 kept constants, but the images are averaged by 10 by the imager. Indeed, the velocity of
212 water movement inside the earth plaster decreases with time, and it becomes sufficiently
213 slow after 3 min in order to allow a reduction of frame speed acquisition without any
214 prejudicial loss of information.

215 After several preliminary tests with pure distilled water, potassium iodide salt was added to
216 the water at a 5% concentration. It increases the attenuation of the signal by the liquid,
217 increasing the gray level difference between the dry earth plaster and material containing
218 water. The presence of water in the earth is then easier to detect by the decrease of the gray
219 value of the pixels in the material.

220 A first program was developed on MATLAB to detect the position of the water front in the
221 earth plaster, allowing the measurement of the depth penetration and the spread of the
222 droplet during the time. The principle of this program is as follow: within a specific region of

interest (ROI), where the droplet spreads, the mean gray level of the pixels is calculated for each horizontal line. An example of this ROI is given by the yellow frame on the Figure 2.

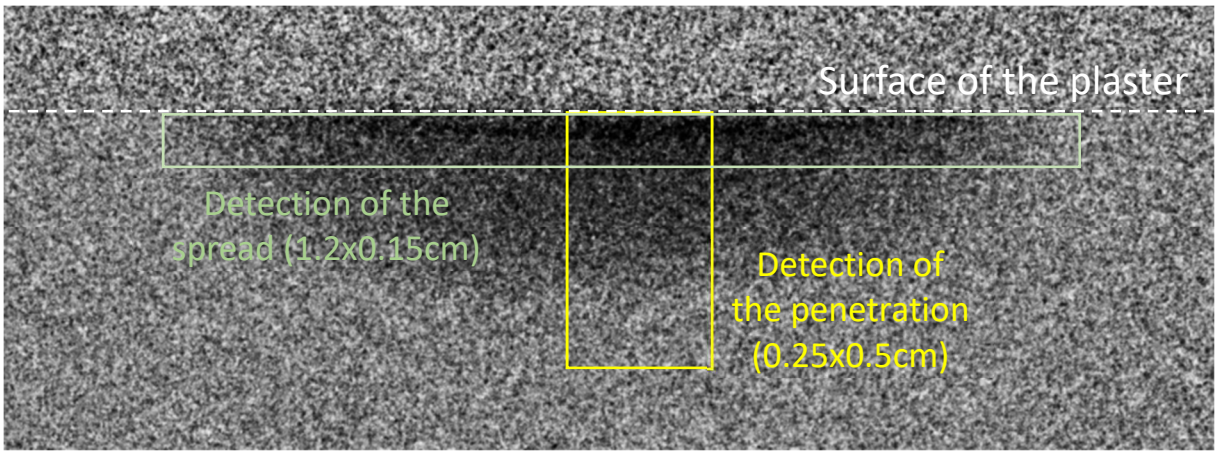

Figure 2: ROIs used for the gray level calculation to detect the position of the water inside the plaster

A reference gray value is set from a dry zone inside the plaster. A threshold is set at ±0.02% of this base value. Then, when the mean grey value calculated from the ROI overcomes this threshold, the position corresponds to the location of the water front inside the material. To illustrate this method, Figure 3 shows the mean gray value for each row of the yellow ROI, from the top (at left; 0 pixels) to the bottom (at right; 220 pixels). One can see that the mean grey value overcomes the threshold around 105 pixels, then the position of the water front is at 105x20 µm = 2.1 mm from the surface of the plaster since the upper side of the ROI corresponds to the surface of the sample.

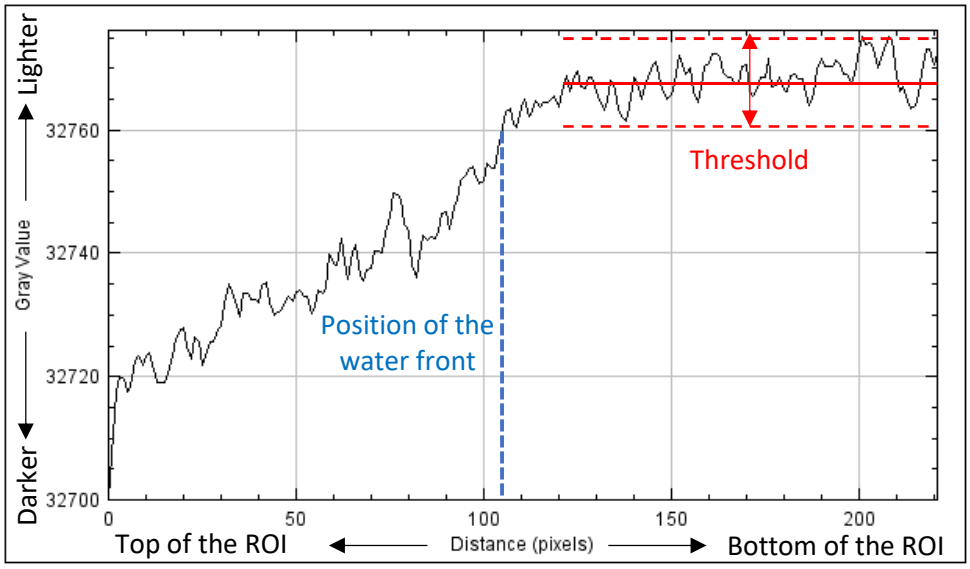

Figure 3: Determination of the water front position with the mean gray value in the yellow ROI (Figure 2) using the threshold

To measure the spreading, the same procedure is used, but the ROI is selected just under the surface of the sample where the droplet impacts, and the calculation is made for vertical lines instead of the horizontal ones. The results here indicate the size of the spread over the time. An example of this ROI is given by the green frame on the Figure 2. Most of the time, the threshold was equal to 0.02% of base gray value from the dry zone. However, for some samples where the noise was too important, the threshold has been set to 0.03%. For different samples, the spread was measured with these two values of threshold, leading to a 2% maximum error on the measurement.

A second MATLAB program was developed to follow the relative quantity of water inside the material. The selected ROI, described on Figure 4, needs to surround all the penetrated droplet, then the mean of the gray level of each pixel of the ROI is calculated. This mean value is calculated over the time and compared to the initial mean gray value, giving a gray

value variation over the time. This allows the observation of the drying phenomenon, and its speed rate. Because the average gray value of the picture drift slightly with time, due to instability of the X-Ray source, a small ROI inside the material is selected, at a location where it is certain that there cannot be water. In this ROI the same calculation is made, and the result, assimilated to a slide, is subtracted to the main gray level variation. With this addition, this code leads finally to the variation of the total gray value of the droplet in the material, which can be representative of the water mass.

This method can be summarized by the following equations. *GVR* is the sum of the pixel's gray value for the droplet's ROI, and *GVD* is the sum of the pixel's gray value for the drift's ROI (i.e. far from the droplet). The suffix "I" refers to the initial value (before the drop of the droplet), the subscript "average" is added when the total gray value (*GVR* or *GDV*) is divided by the number pixel of the considered ROI: $n_{droplet}$ or n_{drift}. Finally, $\Delta GVR_{average}$ is the variation of the average gray value in the droplet's ROI due to the presence of water.

$$GVR_{average} = \frac{GVR}{n_{droplet}} \quad \text{and} \quad GVD_{average} = \frac{GVD}{n_{drift}} \tag{2}$$

$$GVRI_{average} = \frac{GVRI}{n_{droplet}} \quad \text{and} \quad GVDI_{average} = \frac{GVDI}{n_{drift}} \tag{3}$$

$$\Delta GVR_{average} = \left(GVR_{average} - GVRI_{average}\right) - \left(GVD_{average} - GVDI_{average}\right) \tag{4}$$

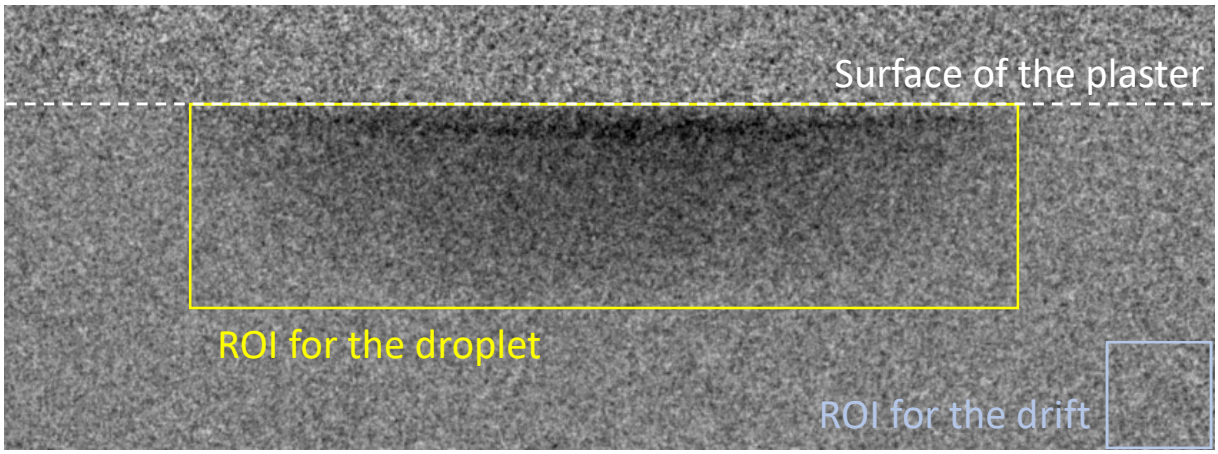

Figure 4: ROIs used to measure the gray variation level over the time (size: 1.2x0.4cm yellow / 0.2x0.2cm blue)

3.2 Water droplet spreading and penetration depth

The X-ray microtomography method developed here aims at understanding the role of the surface and volume on the penetration of a water droplet in earth plasters. Two parameters are obtained from the image analysis described before, the water droplet penetration depth *D* and water droplet spreading *S.* These parameters were monitored over time for all the samples.

A representative example of the results obtained for all the samples is given in Figure 5(a). The penetration depth *D* of the water droplet impacting the surface can be decomposed in two phases. First, a quick increase of *D* during the first seconds is due to the speed of the droplet; here *D* goes from 0 mm to 1 mm within the image rate of 10 fps. Then, following a diffusion process inside a porous material, *D* increases up to 3.5 mm in 400 seconds then stagnates. Note that data are noisier at the beginning due to a smaller acquisition time during the first 3 minutes.

For a better analysis, *D* has been plotted as a function of log(t), as shown on the Figure 5(b). It is worth noting that the initial penetration D_i, which can be extrapolated by the intercept of the regression line, is approximatively equal to 1 mm. The slope of this regression line gives information on the penetration speed of the droplet during the water diffusion phenomenon.

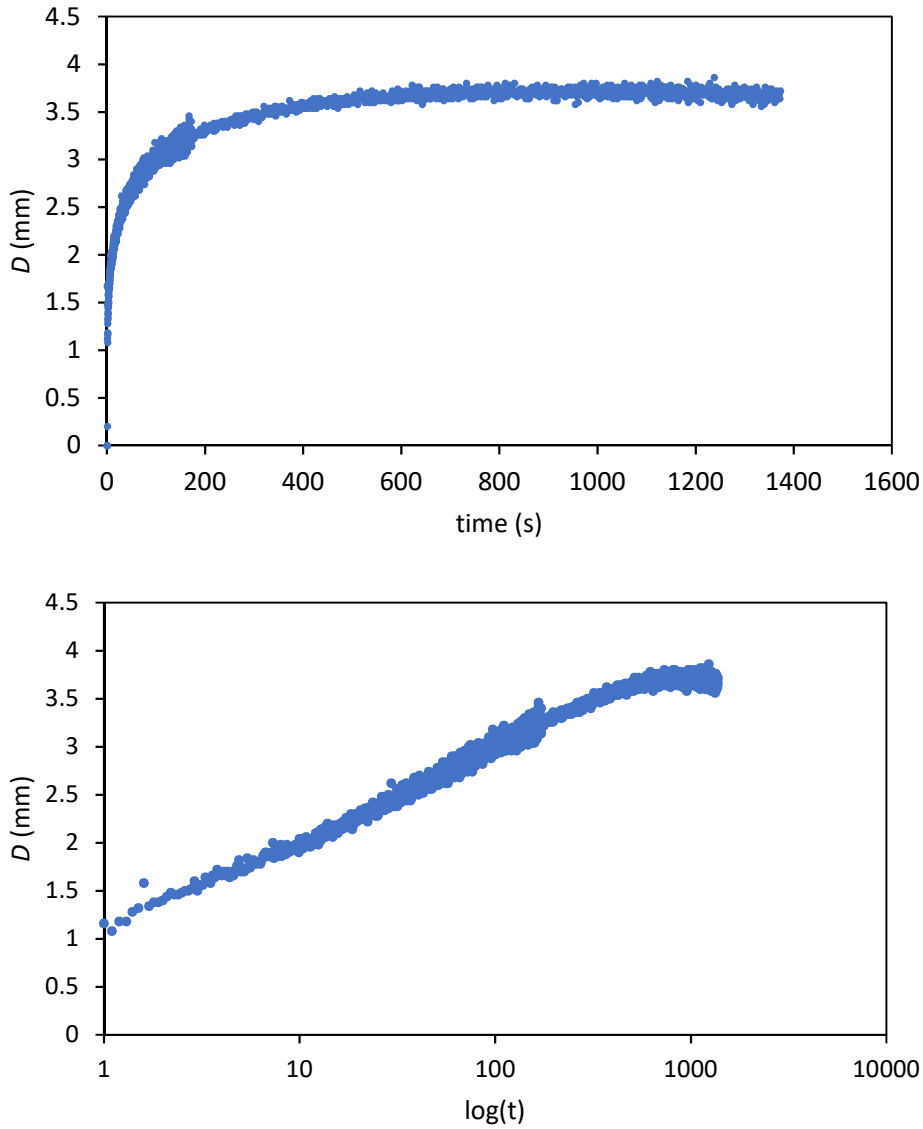

Figure 5: Water depth D over (a,top) time; (b,bottom) log(t) for sample A1 (b,bottom) with regression to intercept the initial depth Di

292 The evolution of the spread *S* is similar of that of depth *D*, as it can be seen on Figure 6(a),
293 with a quick increase from 9 mm to 11.75 mm during the 3 first minutes, followed by a
294 stagnation and even a slight decrease to 11.5 mm. This means that the drying has already
295 started and the water inside the material begins to withdraw on the sides. The initial
296 spreading occurs in a very short time of less than 20 ms [29] that cannot be observed with
297 the acquisition rate of our apparatus. The initial spread S_0 considered here is thus the one
298 when the droplet is pinned to the surface by the capillary forces [29]. It is known from
299 previous work [29] that for an impacting droplet with the same speed and volume, the initial
300 spread is smaller than 9mm. As for *D*, *S* is plotted as a function of log(t) on the Figure 6(b),
301 showing that the speed of the water droplet spreading within the plaster is constant for the
302 first 3 minutes.

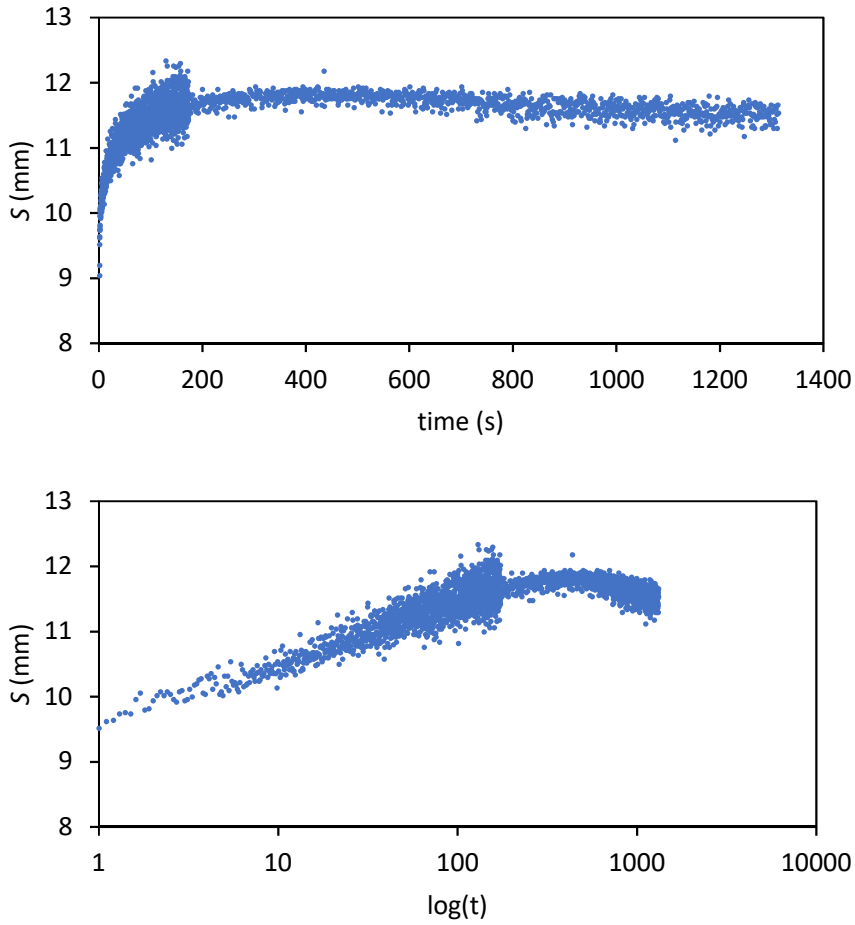

303

304 *Figure 6: Water spread over (a,top) time; (b,bottom) log(t) for sample A1*

305 The Table 4 sums up the results for the final depth penetration D_f and spread S_f for each
306 earth plaster sample. At a first sight these two parameters D_f and S_f vary from one sample to
307 another, with the following tendency: the droplet penetrates deeper for the A series, with
308 lower clay content, higher R_a and A-value; and the droplet spreads more for the B series with
309 higher clay content, lower R_a and A-value. However, a deeper analysis is required to
310 determine if this difference is due to surface properties, volume properties or both.

Sample	**A1**	**A3**	**A5**	**A9**	**B1**	**B1C**	**B1S**	**B2**	**B5**
D_f **(mm)**	3.75	3.75	4.3	3.55	2.9	2.8	1.9	2.75	2.25
S_f **(mm)**	12	11.4	11.4	12.5	13	12.1	13.1	14	13.3

D_f/S_f	0.32	0.35	0.38	0.37	0.25	0.24	0.15	0.22	0.17

Table 4: Parameters D_f and S_f, and ratio D_f/S_f for all the samples

The depth-on-spread ratio D_f/S_f has also been studied in this paper. It is an indicator of the shape of the droplet and how it develops within the earth plaster. Since D_f and S_f vary strongly between the samples, the D_f/S_f is also very different from one sample to another.

3.3 Water drying monitoring

Since the duration of acquisition was 23 minutes and only one droplet has been dropped on the sample, it was possible to observe and monitor the water drying inside the sample, with the method described with (eq.4). Figure 7 shows an application of this method on the representative sample A1. ΔGVR measured the X-ray attenuation due to the water, thus it should be proportional to water mass. At first, an immediate decrease of total intensity signifies that the droplet has penetrated through the surface. Then the drying begins and follows for the entire duration of the experiment the same slope of 0.0043. The drying is not yet over since it should end when the gray variation reaches 0, except modifications to the plaster due to the water droplet.

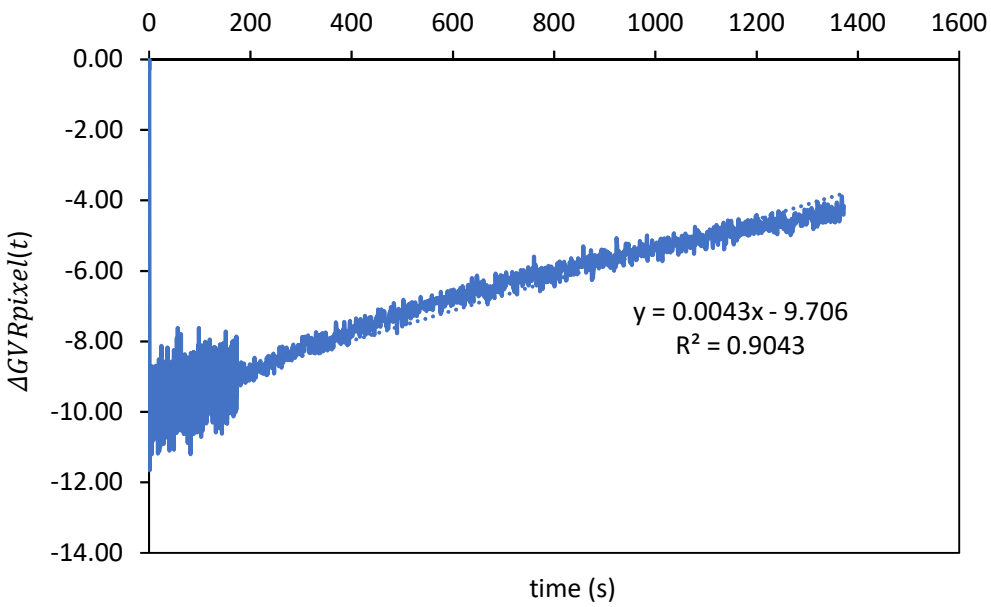

326

327 *Figure 7: Gray value variation over the time per pixel inside the ROI surrounding the droplet*

328 *(see Figure 4) for the sample A1*

329 The drying slope has been normalized by the final dimeter S_f in order to have a drying rate

330 independent of the size of the drying area. Table 5 summarizes the results for all the

331 samples. The drying rate for the A series is considerably higher than the B series, highlighting

332 that the composition of the plaster has a great influence on this drying rate φ.

Sample	**A1**	**A3**	**A5**	**A9**	**B1**	**B1C**	**B1S**	**B2**	**B5**
φ (s^{-1})	3.24E-05	2.56E-05	3.63E-05	2.74E-05	1.69E-05	2.01E-05	2.09E-05	1.88E-05	1.49E-05

333 *Table 5: Drying rate for all the samples*

334

335 **3.4 Pore size determination**

Table 6 presents three levels of porosity. First n_{pycno} is the total porosity of the material, determined experimentally with the pycnometer. However, this technique does not give any information about the pore size distribution. Consequently, a custom MATLAB code has been designed in order to obtain the porosity of the sample from a 3D image. The porosity detected with this method is noted n_{tomo}. Since the pixel size for the experiment was set at 20µm, it is the smallest size of pore that this program is able to detect. Finally, the amount of small pore n_s (<20µm) is the difference between n_{pycno} and n_{tomo}.

Sample	**A1**	**A3**	**A5**	**A9**	**B1**	**B1C**	**B1S**	**B2**	**B5**
n_{pycno} **(%)**	30	32	25	26	26	18	22	26	27
n_{tomo} **(%)**	8	18	21	12	4	8	5	5	3
n_s **(%)**	22	14	4	14	22	10	17	21	24
R_a **(µm)**	16.4	28.7	29.3	23.5	11.7	14.5	9.3	13.8	5.2

Table 6: Three levels of porosity and R_a obtained for all the samples.

The porosity n_{tomo} is quite small compared to n_{pycno}, as only pores larger than 20µm are considered. The largest porosity n_{pycno} was for A1 and A3 sample, due to the worst particle size stacking, stable around 26% for the other ones, and lowest for STA and Confluence earth (samples B1C and B1S). The porosity n_{tomo} for the A series is considerably higher than the B series. In one hand, the role of the granulometry can be easily highlighted: the sample A5, which is composed of the largest sand granulometry, presents a 21% n_{tomo} porosity on its 25% n_{pycno} porosity, therefore only 4% of the pore are under 20 µm. On another hand: the role of the clay is remarkable: the sample B5, which is composed by the largest amount of clay, present only a 3% n_{tomo} porosity on his 27% n_{pynco} porosity, so 24% of the pore are under 20 µm. The roughness R_a has been rewritten in this table in order to compare it to the

results of porosity. It appears that there is a consistent tendency between R_a and n_{tomo}, suggesting that the samples with the highest amount of big size pore are also the roughest.

4 Discussion

In order to understand how the depth-on-spread D_f/S_f ratio is related to the material by a surface or volume effect, it is plotted versus the R_a values on Figure 8(a), and versus the A-value values, on Figure 8(b) for all the samples. The R_a is a surface parameter whereas the A-value depends more on the volume composition of the sample (granulometry, % of earth, porosity…).

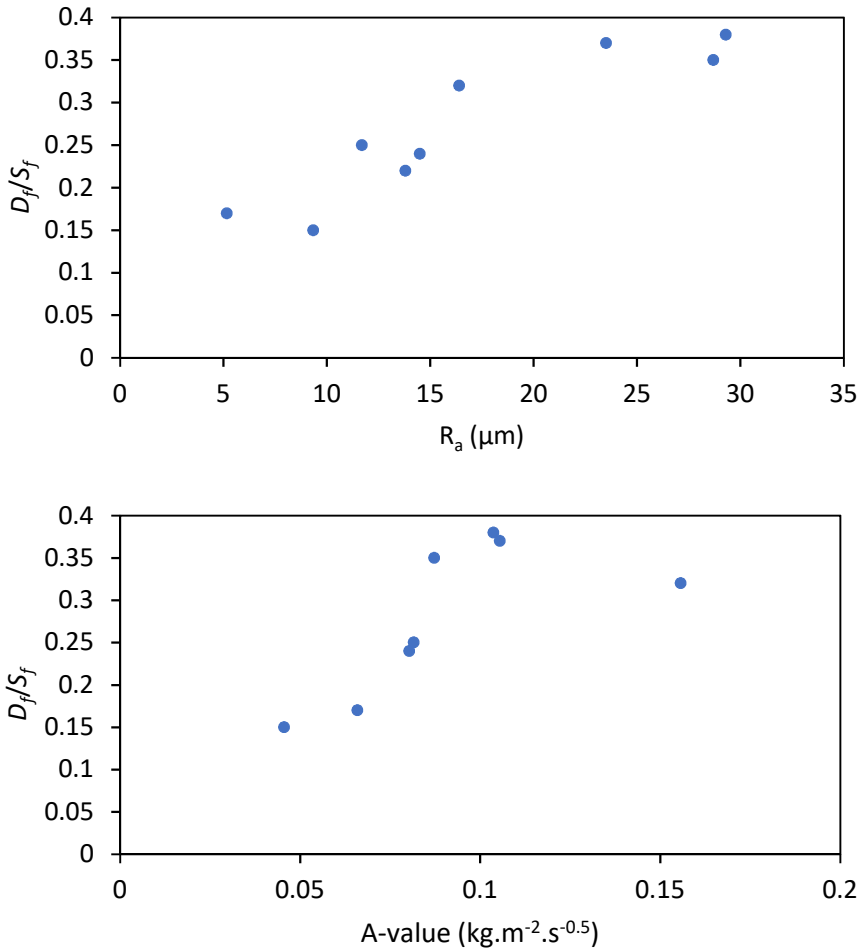

363

364 *Figure 8: (a, top) ratio D_f/S_f over surface parameter R_a; (b, bottom) D_f/S_f over volume*

365 *parameter A-value for all the samples*

366 Both R_a and *A-value* seem to have an influence on the *D/S* ratio. The hypothesis proposed

367 here is that the final ratio D_f/S_f is driven by both surface and volume phenomenon, but at

368 different timescales.

369 First, when the water droplet impacts the surface, it spreads over it and some of the water

370 penetrates into the material in a very short time (<1sec (log1)) due to inertial effects. The

371 kinetic energy of the water droplet forces it to penetrate through the porosity, while the

372 friction of the water around the pores restrains its movement.

As supposed by Lee *et al.* in [30], the inertial effect can be estimated as a volume of water with density ρ penetrating a cylindrical pore of radius R at a depth z with a speed V_i. Then the movement quantity in this liquid is given by:

$$P_L = \pi R^2 z \rho V_i \tag{5}$$

While the liquid of viscosity μ is restrained by the viscous force f_f which works on the sides of the cylindrical pore (area A = 2πR) for a time $\tau \approx z/V_i$. Then the movement quantity restrained by this force is given by:

$$f_f = \mu \frac{V_i}{R} \tag{6}$$

$$P_f = A f_f \tau \approx 2\pi z^2 \mu \tag{7}$$

Since the capillary effects can be neglected at this scale of time, the depth penetration z can be expressed by equating (eq.5) and (eq.7), as follows:

$$z \approx V_i \frac{\rho R^2}{\mu} \tag{8}$$

In this study, for a 1 m/s water droplet speed, which has penetrated 2.5 mm inside the plaster in a very short time, estimated to 2.5 ms (sample A3), the equivalent pore radius equals to around 50 µm. In another hand, for a water droplet which has penetrated 0.5 mm inside the plaster in 0.5 ms, the equivalent pore radius is around 25 µm.

Then, (eq 8) shows that the larger the pore size is, the deeper the water penetrates because there is less friction. As remarked in (3.4), in this case the big size pores are also correlated with the roughness of the surface. Consequently, the depth penetration z, which can be assimilated to D_i, should scale with R_a as confirmed on Figure 9. Because the initial depth D_i

393 is so different between the samples, it explains why the final D_f/S_f ratio is larger for the A
394 series, whose samples present a higher roughness than the B series.

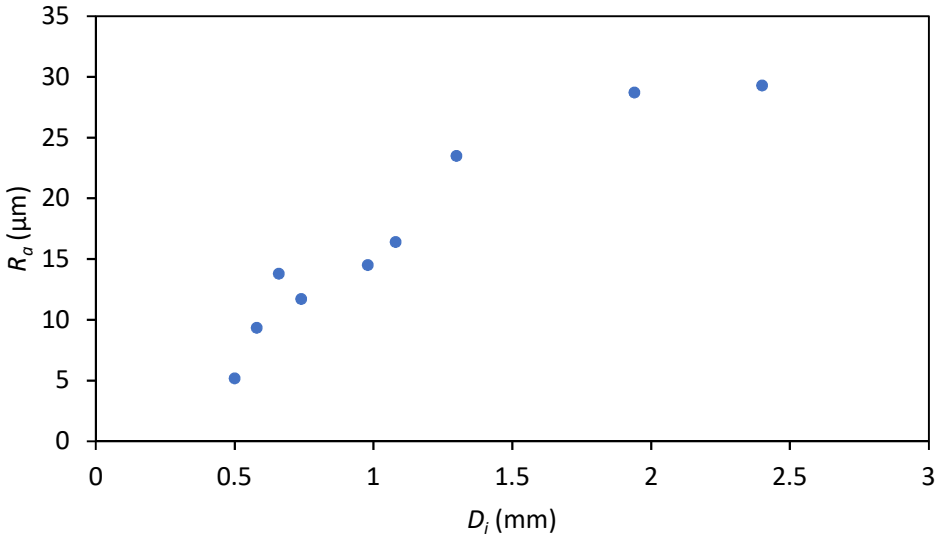

395

396 *Figure 9: Initial water depth penetration D_i compared to Ra for all the samples*

397 In a second time, the penetration of the water when the inertial effects are overcome
398 depends only on the efficiency of the material composition to diffuse water, with influence
399 of the clay content, granulometry, density, porosity… This efficiency was measured with the
400 *A-value* test. The initial depth penetration D_i was subtracted to the final depth penetration
401 D_f to obtain only the depth penetration due to water diffusion. When this $(D_f\text{-}D_i)/S_f$ ratio is
402 plotted with the *A-value*, as on the Figure 10, it confirms that the behavior of the liquid after
403 impact is only driven by the efficiency of the material to conduct water.

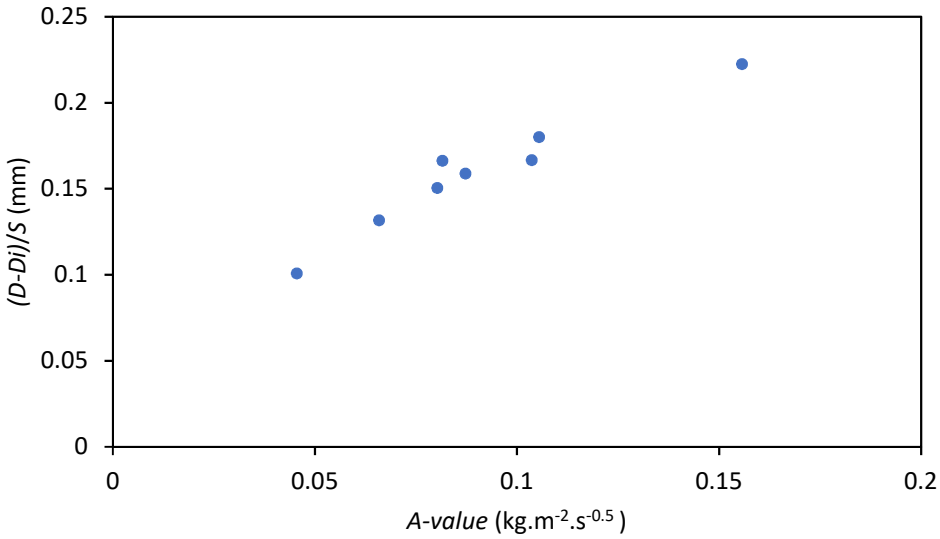

404

405 *Figure 10: New ratio without initial penetration D-Di/S compared to volume parameter A-*

406 *value for all the sample*

407 Both surface and bulk properties influence on the water droplet penetration have been
408 demonstrated on Figure 9 and 10. However, both effects are related to the initial spreading
409 S_i of the droplet. Indeed, the water droplet spreads on the surface at impact until the
410 capillary forces at the sample's surface pin the contact line [29]. At this moment, the droplet
411 depletes while keeping its spread diameter constant until there is no water left above the
412 surface, as explained in [29]. This spreading diameter is considered as the initial spread S_i
413 and is directly connected to the surface roughness R_a, as shown on Figure 11. For the very
414 rough samples, the water droplet requires more energy to pass the obstacles of the surface
415 topography and the water is quickly trapped into high open porosity. At the opposite, for the
416 smoother samples, the water droplet slides easily until the capillary forces overcome the
417 kinetic energy, pining the droplet. In between, the behavior of the water droplet is more
418 complex, since the spreading depends also on the air film trapped between the droplet and
419 the surface [30].

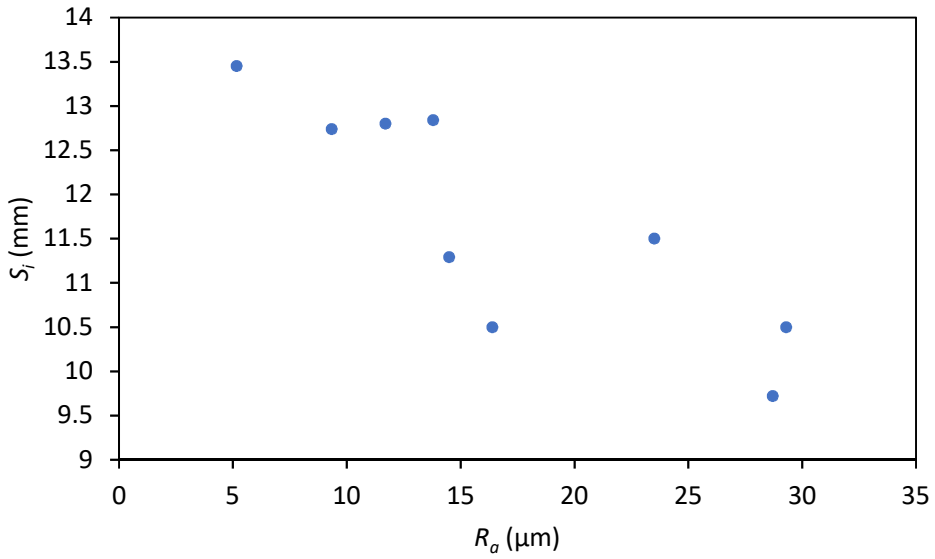

420

421 *Figure 11: Initial spread S_I compared to surface parameter R_a for all the samples*

422 Then, while the initial spread S_i depends on the surface topography of the sample, it leads to
423 a different water droplet area, which consequently provides a greater surface for the water
424 to diffuse into the material. Because the water droplet volume is equal for all samples, the
425 surface topography modifies the final result D_f/S_f.

426 To observe only the water diffusion in the material, it is necessary to normalize by the initial
427 spread S_i. The Figure 13 presents the ratio D/S_i plotted by S/S_i followed over the time for all
428 the samples. The curves are compared to the analytic solution of the Weber's disc diffusion,
429 from [31]. This analytical solution describes the diffusion for a disc of liquid of initial radius a
430 with a concentration of 1 at the surface of a semi-infinite media with a concentration of 0.
431 The schema of this problem is presented on Figure 12. The red line represents the water
432 front.

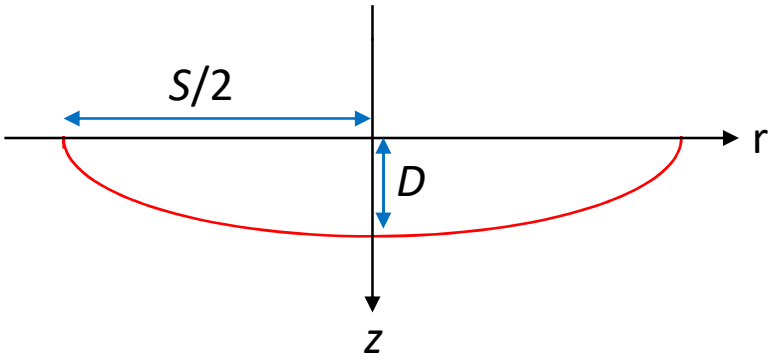

433

434 *Figure 12: schema of the Weber's disc problem*

435

436 The iso-values are equal to:

437 $$(r^2 + z^2 - a^2) + \sqrt{(r^2 + z^2 - a^2)^2 + 4a^2z^2} = cst \quad (9)$$

438 The iso-value which delimitates the droplet is the one for which *a* would be equal to the half

439 of the initial spread ($a = S_i/2$). At z = 0, r would be equal to the half of the current spread (r

440 = *S*/2 at *z* = 0). Finally, at r = 0, z would be equal to the penetration depth (z = D at r = 0).

441 Using these notations, the eq. (9) provides:

442 $$\frac{S}{S_i} = \sqrt{4\frac{D^2}{{S_i}^2} + 1} \quad (10)$$

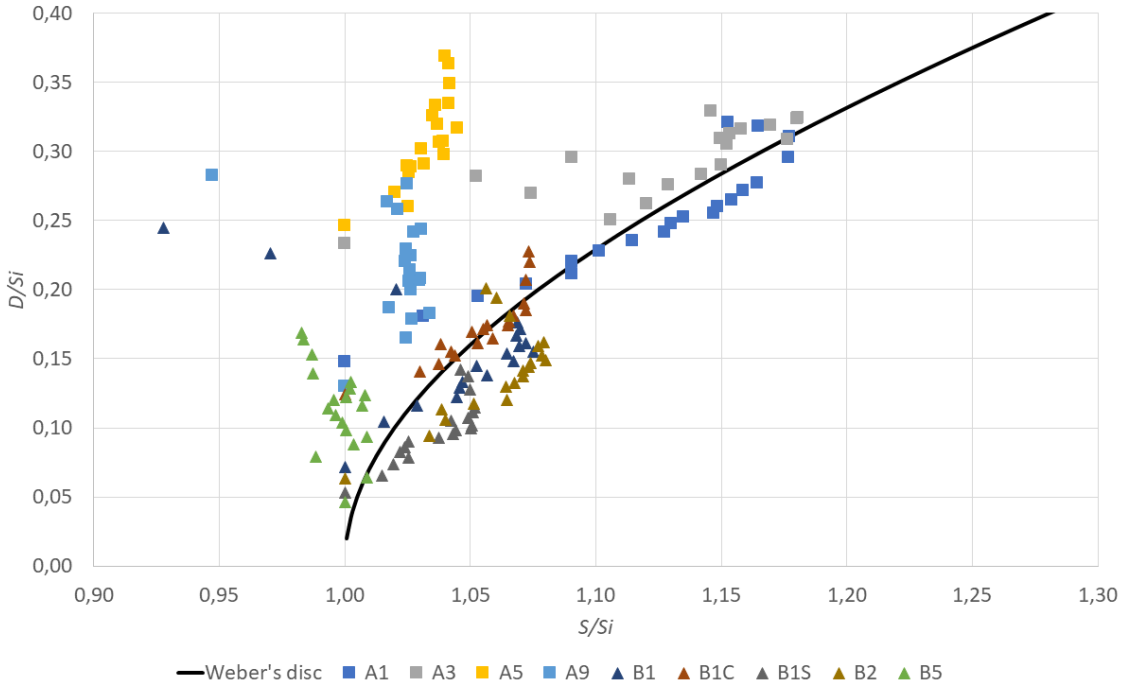

443

444 *Figure 13: Evolution of D compared to evolution of S and normalized by S_i for all the sample,*

445 *compared to Weber's disc solution's iso-values (9)*

446 On Figure 13, one can notice a consistent fit between the weber's disc solution and the
447 experiment for most of the samples. Although, the samples A5, A9, and B5 do not follow the
448 analytical solution. Indeed, their behaviors represent an important evolution of the depth
449 penetration *D* compared to the spreading diameter *S*. A5 and A9 are the roughest samples
450 with the larger pore size due to their large sand granulometry. As a consequence, water can
451 easily penetrate the material through large porosities. This plus the small initial spreading S_i
452 can explain this evolution out of the analytical solution. For B5, the initial spread S_i is very
453 important due to the smooth surface, then the evolution of S/S_i is very weak.

454 Then, the analytic solution of Weber's disc is not followed for extreme behaviors due to a
455 very particular composition (high granulometry or high clay content) leading to extreme
456 boundaries at the surface. On the contrary the other samples are well described by the iso-
457 value obtained with the Weber's disc analytic solution (eq.9).

Figure 13 also shows the beginning of the drying. As an example, for the samples A1, A9, B1, it can be noticed that the last points of the curve present an important reduction of the ratio S/S_i, which means that the water front inside the plaster is withdrawing. It is worth noting that, in this particular study, the origin of the earth has less influence on the water droplet penetration compared to the initial penetration D_i or initial spreading S_i.

Overall, it can be interesting to note that the earth plasters with a finer sand granulometry and a higher clay proportion prevent the water droplet to penetrate too deeply under the surface, which can be convenient for a coating material. However, when looking at the drying rate φ (3.3) function of the ratio D_f/S_f for all the sample, presented on Figure 14, it appears also that the samples with the highest D_f/S_f ratio, are also the ones which dry the faster. The earth plasters in which the water penetrates the deeper are also the ones which dry the faster, which can also present a certain benefit for a coating material.

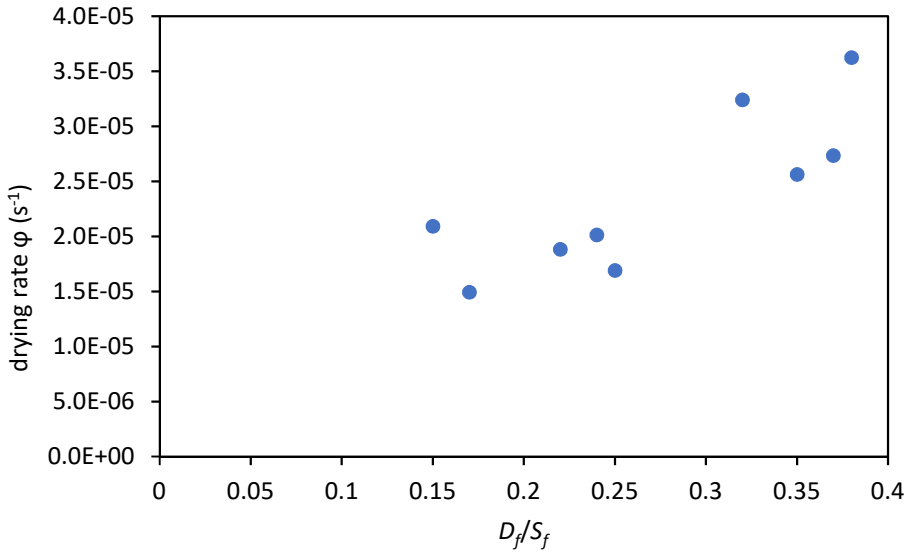

Figure 14: Drying rate compared to ratio D_f/S_f for all the samples

5 Conclusion

An original experimental protocol of droplet damping followed by X-ray microtomography was designed to analyse the behavior of an impacting water droplet penetrating inside several earth plasters. Through the development of specific settings, it was possible to capture clearly the water droplet penetration in the earth plaster at a speed up to 10 fps with a 20 µm resolution. Two custom MATLAB codes were developed to follow the shape of the droplet, and the relative quantity of water inside the material.

The earth plasters were prepared with a specific protocol, with variable earth origin and sand granulometry, to obtain great variations of surface parameters such as roughness R_a, and volume parameters such as density, A-value, porosity. This variety of composition leading to a great spread of surface and volume parameter values, it highlighted for the first time to our knowledge the influence of both surface and volume on the penetration of the water droplet in such material. During the impact of the droplet, a rough surface topography conducts to a smaller initial water droplet spreading and a deeper initial water penetration. When the inertial effects are overcome, the water diffuses into the earth plasters following the analytic solution of Weber's disc, except for the most extreme compositions. In order to enhance the comprehension of the role of the sand granulometry and the clay in the penetration of the water, further work should be conducted on theses extreme compositions.

The information given by the X-ray microtomography experiment are particularly adapted to the design of an efficient earth plaster. Indeed, the direct observation of the water inside the plaster, in terms of shape and relative quantity, will enable the determination of the best compromise between a low penetration and a quick drying. Or, according to local and

specific constraints, the choice of one on another phenomenon can be preferred in the design of the plaster. Then, it could be for example a tool to master the thickness of the earth plaster.

It has been shown that the modification of the plaster surface topography can give some control over the penetration of the water droplet. However, it is not yet known how this surface topography will be transformed by the repeated impacts of droplets over the time, and if these results will remain in such conditions. This leads also to an interrogation about the durability of theses earth plasters under repeated water exposition, as in rooms with water use, work which will be done in further experiments.

Earth plasters coated with hydrophobic products, as bio-polymers, to enhance their action against water erosion may also benefits from this new experiment, as it may improve the understanding of the water behavior under the coated surface, and control precisely the amount of water penetrating trough the surface.

Acknowledgment

The authors would like to thank D. Hautemayou and C. Mézière from Laboratoire Navier for designing the setup on the microtomograph.

E. Keita work has been carried out in the framework of Alluvium, an I-SITE FUTURE project funded by the French Research Agency.

References

517 [1] Hammond, G.P., Jones, C.I, 2008. Embodied Energy and Carbon in Construction Materials.
518 Proceedings of the Institution of Civil Engineers. Energy. 161, 87-98.

519 [2] Morel, J.C., Mesbah, A., Oggero, M., Walker, P., 2011. Building Houses with Local
520 Materials: Means to Drastically Reduce the Environmental Impact of Construction.
521 Construction and Building Materials. 36, Issue 10, 1119-1126.

522 [3] McGregor, F., Heath, A., and Shea, A., 2014. The Moisture Buffering Capacity of Unfired
523 Clay Masonry. Building and Environment. 82, 599–207.

524 [4] Labat, M., Magniont, C., Oudhof, N., Aubert, J., 2016. From the Experimental
525 Characterisation of the Hygrothermal Properties of Straw-Clay Mixtures to the Numerical
526 Assessment of its Buffering Potential. Building and Environment. 97, 69–81.

527 [5] Soudani, L., Woloszyn, M., Fabbri, A., Morel, J. C., Grillet, A. C., 2017. Energy Evaluation of
528 Rammed Earth Walls Using Long Term In-Situ Measurements. Solar Energy. 141, 70–80.

529 [6] Santos, T., Gomes, M., Santos Silva, A., Ferraz, E., Faria, P., 2020. Comparison of
530 Mineralogical, Mechanical and Hygroscopic Characteristic of Earthen, Gypsum and Cement-
531 Based Plasters. Construction and Building Materials. 254, 1-11.

532 [7] Bui, Q. B., Morel, J. C., Venkatarama Reddy, B. V., Ghayad, W., 2009. Durability of
533 Rammed Earth Walls Exposed for 20 Years to Natural Weathering. Building and
534 Environment, 44, 912–919.

535 [8] Champiré, F., Fabbri, A., Morel, J. C., Wong, H., McGregor, F., 2016. Impact of Relative
536 Humidity on the Mechanical Behavior of Compacted Earth as a Building Material.
537 Construction and Building Materials, 110, 70–78.

538 [9] Bruno, A., Perlot, C., Mendes, J., Gallipoli, D., 2018. A Microstructural Insight into the
539 Hygro-mechanical Behaviour of a Stabilised Hypercompacted earth. Materials and
540 Structures, 51, 32.

541 [10] Delinière, R., Aubert, J.E., Rojat, F., Gasc-Barbier, M., 2014. Physical, Mineralogical and
542 Mechanical Characterization of Ready-Mixed Clay Plaster. Building and Environment. 80, 11-
543 17.

544 [11] Emiroğlu, M., Yalama, A., Erdoğdu Y., 2015. Performance of Ready-Mixed Clay Plasters
545 Produced with Different Clay/Sand Ratios. Applied Clay Science. 115, 221-229.

546 [12] Santos, T., Nunes, L., and Faria, P., 2018. Production of Eco-Efficient Earth-Based
547 Plasters: Influence of Composition on Physical Performance and Bio-Susceptibility. Journal of
548 Cleaner Production. 167, 55–67.

549 [13] Faria, P., Tânia Santos, T., Aubert, J. E., 2016. Experimental Characterization of an Earth
550 Eco-Efficient Plastering Mortar. Journal of Materials in Civil Engineering. 28, Issue 1.

551 [14] Randazzo, L., Montana, G., Hein, A., Castiglia, A., Rodonò, G., Donato, D.I., 2016.
552 Moisture Absorption, Thermal Conductivity and Noise Mitigation of Clay Based Plasters: the
553 Influence of Mineralogical and Textural Characteristics. Applied Clay Science. 132–133, 498-
554 507.

555 [15] Stazi, F., Nacci, A., Tittarelli, F., Pasqualini, E., Munafò, P., 2016. An Experimental Study
556 on Earth Plasters for Earthen Building Protection: the Effects of Different Admixtures and
557 Surface Treatments. Journal of Cultural Heritage, 17, 27-41.

558 [16] Lima, J., Faria, P., Santos Silva, A., 2020. Earth Plasters: The Influence of Clay Mineralogy
559 in the Plasters' Properties. International Journal of Architectural Heritage. 14, 948-963.

560 [17] Fabbri, A., Soudani, L., McGregor, F., Morel, J. C., 2019. Analysis of the Water Absorption
561 Test to Assess the Intrinsic Permeability of Earthen Materials. Construction and Building
562 Materials. 199, 154–162.

563 [18] Marmur, A., 1989. Capillary Rise and Hysteresis in Periodic Porous Media. Journal of
564 Colloid and Interface Science. 129, 278–285.

565 [19] Denesuk, M., Smith, G. L., Zelinski, B. J., Kreidl, N. J., Uhlmann, D. R., 1993. Capillary
566 Penetration of Liquid Droplets into Porous Materials. 158, 114-120.

567 [20] Lee, J. B., Derome, D., Dolatabadi, A., Carmeliet, J., 2016. Energy Budget of Liquid Drop
568 Impact at Maximum Spreading: Numerical Simulations and Experiments. Langmuir, 32,
569 1279–1288.

570 [21] Lee, J. B., Derome D., Guyer, R., Carmeliet, J., 2016. Modeling the Maximum Spreading
571 of Liquid Droplets Impacting Wetting and Nonwetting Surfaces. Langmuir. 32, 1299–1308.

572 [22] Parracha, J. L., Pereira, A., Velez da Silva, R., Almeida, N., Faria, P., 2019. Efficacy of Iron-
573 Based Bioproducts as Surface Biotreatment for Earth-Based Plastering Mortars. Journal of
574 Cleaner Production. 237, 117803.

575 [23] Keita, E., Kodger, T. E., Faure, P., Rodts, S., Weitz, D. A., Coussot, P., 2016. Water
576 Retention against Drying with Soft-Particle Suspensions in Porous Media. Physical Review. E
577 94.

578 [24] Keita, E., Faure, P., Rodts, S., and Coussot, P., 2013. MRI Evidence for a Receding-Front
579 Effect in Drying Porous Media. Physical Review. E 87.

580 [25] Massoussi, N., Keita, E., Roussel, N., 2017. The Heterogeneous Nature of Bleeding in
581 Cement Pastes. Cement and Concrete Research**,** 95, 108-116.

582 [26] Houben, H., Guillaud, H., 2006. Traité De Construction En Terre. CRATerre.

583 [27] NF EN ISO 17892-4. Geotechnical Investigation and Testing - Laboratory Testing of Soil -
584 Part 4 : Determination of Particle Size Distribution. French Standard. AFNOR. January 2018.

585 [28] NF EN 1015-18. Methods of Test for Mortar for Masonry - Part 18 : Determination of
586 Water Absorption Coefficient due to Capillary Action of Hardened Mortar. French Standard.
587 AFNOR. May 2003.

588 [29] Mauffré, T., McGregor, F., Contraires, E., Fabbri, A., 2019. Influence of Walls Surface
589 Topography on Water Droplet Damping and Absorption for Earthen Constructions. Building
590 and Environment. 166, 106395.

591 [30] Lee, J. B., Derome, D., Carmeliet, J., 2016. Drop Impact on Natural Porous Stones.
592 Journal of Colloid and Interface Science. 469, 147–156.

593 [31] Crank, J., 1975. The Mathematics of Diffusion. Oxford University press. Second edition,
594 London, pp. 42-43 (Chapter 3).